Po-Yi Lee
Department of Bioengineering,
Swanson School of Engineering,
Pittsburgh, PA 15213;
Department of Ophthalmology,
School of Medicine,
University of Pittsburgh,
Pittsburgh, PA 15213

Yi Hua
Department of Ophthalmology,
School of Medicine,
University of Pittsburgh,
Pittsburgh, PA 15213

Bryn L. Brazile
Department of Ophthalmology,
School of Medicine,
University of Pittsburgh,
Pittsburgh, PA 15213

Bin Yang
Department of Ophthalmology,
School of Medicine,
University of Pittsburgh,
Pittsburgh, PA 15213;
Department of Engineering,
Rangos School of Health Sciences,
Duquesne University,
Pittsburgh, PA 15219

Lin Wang
Devers Eye Institute,
Portland, OR 97210

Ian A. Sigal[1]
Department of Bioengineering,
Swanson School of Engineering,
Pittsburgh, PA 15213;
Laboratory of Ocular Biomechanics,
Department of Ophthalmology,
School of Medicine,
University of Pittsburgh,
203 Lothrop Street,
Eye and Ear Institute,
Rm. 930,
Pittsburgh, PA 15213
e-mail: ian@OcularBiomechanics.com

A Workflow for Three-Dimensional Reconstruction and Quantification of the Monkey Optic Nerve Head Vascular Network

A comprehensive characterization of the three-dimensional (3D) vascular network of the optic nerve head (ONH) is critical to understanding eye physiology and pathology. Current in vivo imaging technologies, however, do not have simultaneous high spatial resolution and imaging depth to resolve the small vessels deep within the ONH. We describe a workflow for the 3D reconstruction and quantitative morphological analysis of the ONH vasculature. The vessels of a normal monkey ONH were perfusion labeled. Serial cryosections of the ONH were imaged using fluorescence microscopy (FM) and instant polarized light microscopy (IPOL) to visualize the labeled vessels and label-free collagen, respectively. The IPOL images were registered and used to form a stack of FM images from which the vessels were segmented and skeletonized to reconstruct the 3D vascular network. The network consisted of 12,966 vessel segments, 7989 branching points, and 1100 terminal points at the boundaries. For each vessel segment, we measured its length, tortuosity, inclination (θ), and polar orientation (φ). The length followed a lognormal distribution, whereas the distribution of the tortuosity followed an exponential decay. The vessels were mainly oriented toward the coronal plane ($\theta = 90$ deg). For orientation, there were nearly as many vessels aligned circumferentially ($\varphi = 90$ deg) and radially ($\varphi = 0$ deg). Our results demonstrate the workflow for 3D eye-specific reconstruction and quantification of the monkey ONH vascular network. This is a critical first step to analyze the blood flow and oxygenation within the ONH, which will help understand the role of vascular dysfunction in glaucoma. [DOI: 10.1115/1.4054056]

Keywords: optic nerve head, vasculature, tortuosity, perfusion, fluorescence

1 Introduction

Glaucoma is a leading cause of blindness worldwide [1]. It is characterized by irreversible damage to the retinal ganglion cell axons within the optic nerve head (ONH), specifically within the lamina cribrosa (LC) (Fig. 1). The blood vessels of the ONH form a complex network intertwined with the collagen beams in the LC [2,3]. The primary risk factor for axon damage is an elevated intraocular pressure [4–10]. However, the level of intraocular pressure that causes axon damage varies substantially between people, with a large number of patients suffering axon loss at apparently normal levels of intraocular pressure [9,10]. The evidence thus indicates that there are other factors contributing to

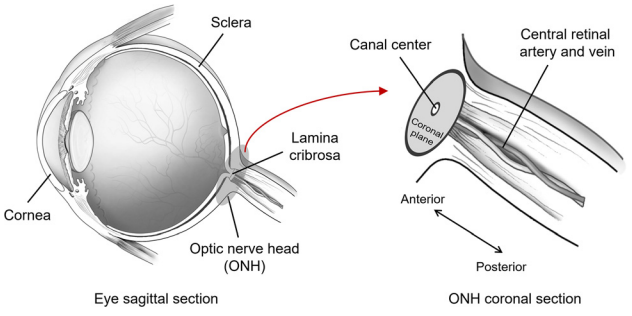

Fig. 1 Diagram of the eye with defined anterior-posterior direction and coronal plane. Adapted from a diagram by the National Eye Institute.

[1]Corresponding author.

Manuscript received November 16, 2021; final manuscript received March 2, 2022; published online March 24, 2022. Assoc. Editor: Craig Goergen.

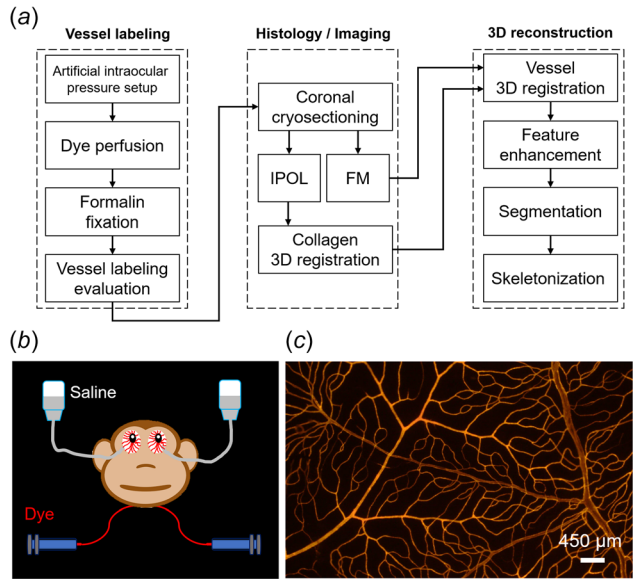

Fig. 2 (*a*) Flow chart of the 3D reconstruction process of an eye-specific vascular network in a monkey ONH (simplified to the key steps). (*b*) Illustration of the perfusion setup for dye perfusion. Two microcatheters were inserted into the carotid arteries on each side of the neck of a monkey for dye perfusion and formalin fixation. A set of isotonic saline columns were used to control the intraocular pressure of the eyes. (*c*) Example FM image of the vessels in the retina. The image shows continuous staining of the retinal vasculature without any discernible dark patches or leaks, suggesting the eye had satisfactory posterior pole perfusion and was, therefore, a candidate for cryosectioning and reconstruction. A second vessel labeling evaluation was done after the vessel 3D registration to confirm good quality labeling of ONH vessels (see Fig. 3).

axon loss and vision loss in glaucoma. It has long been believed that axon damage could also result from an insufficient oxygen supply within the ONH due to compromised blood flow [11–15].

To understand the hemodynamic environment within the ONH and the potential role of blood flow and the oxygen supply, a critical first step is to visualize and characterize its three-dimensional (3D) vascular network. The vessels of the ONH can be fairly small—10 to 20 μm in diameter, and deep—several hundred micrometers from the optic disk surface [2,15]. In addition, some of the vessels are enclosed within collagen beams [2,16]. Current tools for visualizing posterior pole vasculature in vivo do not have sufficient resolution or imaging depth [16]. For example, optical coherence tomography angiography has a high spatial resolution and provides excellent data on the retina and in some small regions of the LC [17–19]. However, it does not have sufficient imaging depth to visualize the vessels deep inside the ONH. Ultrasound and magnetic resonance imaging have a high imaging depth but do not have the spatial resolution necessary to discern the small vessels of the ONH [20–27]. Because of the importance of characterizing the ONH vasculature, there have been many attempts to do that ex vivo. One of the most successful was the use of vascular castings, often made in plastic [28,29]. Analysis of the vascular casts, however, required destroying the rest of the tissues using corrosion methods, which precludes precisely identifying the location of vessels relative to known nonvessel components, such as the collagen. Given the limitations of in vivo imaging and plastic casts, histological imaging remains a powerful alternative to visualize the vessels of the ONH. It allows for high spatial resolution imaging, and the depth of study is only a matter of studying enough sections.

Our goal was to develop a histological imaging workflow allowing reconstruction and quantitative morphological analysis of the full 3D vascular network of the ONH. The workflow should allow visualization of nonvascular tissues for context, and the reconstruction and analysis include deep tissues within and behind the LC and feeder vessels in the peripapillary sclera. Based on the reconstructed vascular network, we measured for each vessel segment four geometric parameters: length, tortuosity, inclination, and polar orientation. The workflow demonstrated herein is a prerequisite to assess the hemodynamic environment within the ONH, which will help clarify the underlying mechanisms of retinal ganglion cell axon damage in ischemic-related ocular diseases such as glaucoma.

2 Methods

First, we reconstructed the 3D vascular network of the ONH following the general procedure shown in Fig. 2(*a*). Then, we characterized four geometric parameters for each of the vessel segments: length, tortuosity, inclination, and polar orientation. The steps are described in detail below.

2.1 Vessel Labeling. All procedures were approved by the University of Pittsburgh's Institutional Animal Care and Use Committee (IACUC) and adhered to both the guidelines set forth in the National Institute of Health's Guide for the Care and Use of Laboratory Animals and the Association of Research in Vision and Ophthalmology Statement for the use of animals in ophthalmic and vision research [30].

The head of a healthy 15-year-old female rhesus macaque monkey was received within 30 min of sacrifice. Two polyimide microcatheters (Doccol Inc., Sharon, MA) were inserted into the carotid arteries on each side of the neck. The vascular bed was washed with warm phosphate-buffered saline. To avoid vessel

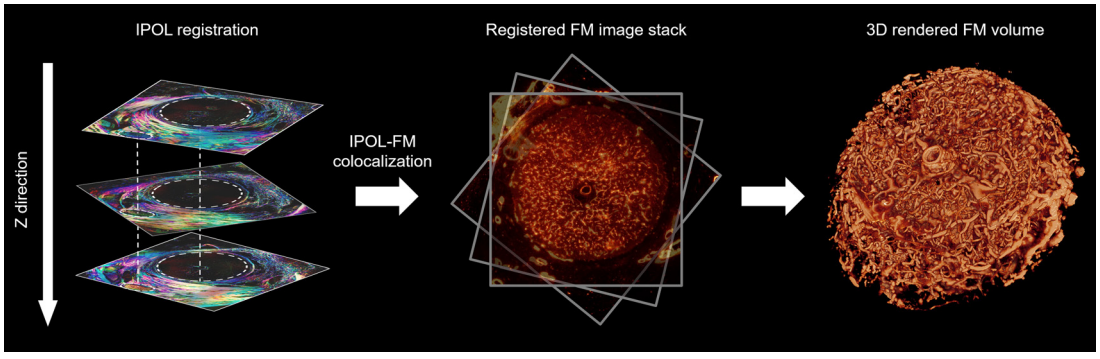

Fig. 3 Illustration of the 3D vessel reconstruction. Left. The stack of IPOL images was registered manually based on tissue edges and features (white dashed circles). Middle. The transformations (translations and rotation) from IPOL image registration were applied to the stack of FM (vascular) images. Right: 3D rendering of the ONH vasculature.

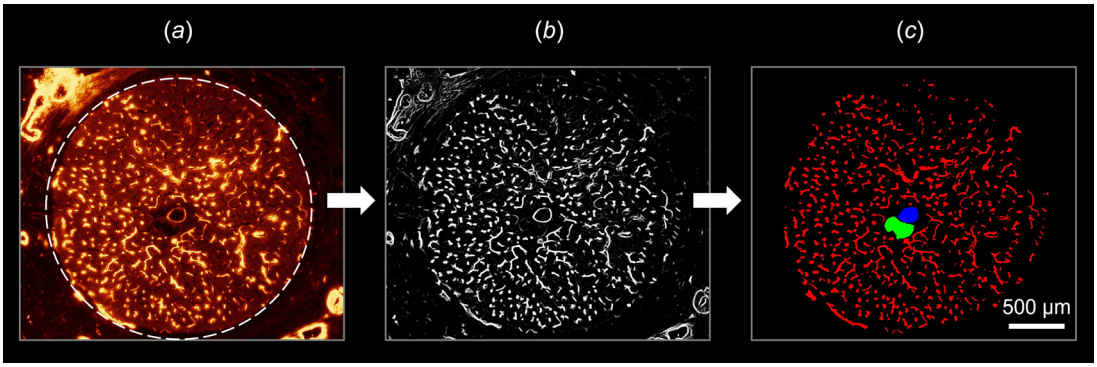

Fig. 4 Vessel segmentation. (*a*) Example FM image of a coronal section through the ONH. Vessels are shown in bright yellow. The white dashed line illustrates the boundary of the scleral canal (exact canal boundaries were obtained from the IPOL images). (*b*) A Frangi filter was used to enhance the vascular features and reduce the background noises on the FM image. (*c*) The feature-enhanced vessels were segmented using the hysteresis thresholding method, and the segmentations were manually checked. We focused on the vessels within the scleral canal. Red—ONH vessels within the canal, blue—central retinal artery, green—central retinal vein: (*a*) FM image, (*b*) feature enhancement, and (*c*) segmentation. (Color version online.)

damage, the phosphate-buffered saline perfusion pressure was first minimal, and then progressively increased over several minutes as the output solution cleared. Phosphate-buffered saline was washed for at least 10 min after the output was clear. The anterior chamber of each eye was cannulated to control intra-ocular pressure using an isotonic saline fluid column. The intraocular pressure was set to 5 mmHg throughout the experiment. The level was selected as a compromise to be as low as possible to minimize intraocular pressure-induced vessel closure, without being so low as to causing buckling or hypotony that could distort the tissues. DiI, a lipophilic carbocyanine dye, was used to label vessels in the eye [31]. We perfused 100 mL of aqueous Dil solution into each carotid artery at a rate of 5–10 mL/min until the whole solution had been used (about 12 min), followed by another phosphate-buffered saline wash to remove residual DiI.

We then perfused 50 mL of 10% formalin into each carotid artery twice, with an interval of 15 min, while maintaining intraocular pressure at 5 mmHg. After an additional 15 min, both eyes were enucleated, making sure to preserve optic nerves at least 5 mm in length from the globe. The intraocular pressure control lines were switched from saline to 10% formalin columns. To complete the fixation, both eyes were immersion fixed overnight in 10% formalin while the intraocular pressure was maintained at 5 mmHg.

The right eye was hemisected, and the retina was examined under a dissecting fluorescence microscope (Olympus MVX10, Olympus, Tokyo, Japan) to evaluate vessel labeling. Although a perfectly labeled retina is not equivalent to a perfectly labeled ONH, perfusion problems often show up in both regions and are easier to spot in the retina. The image shows continuous staining of the retinal vasculature without any discernible dark patches or leaks (Fig. 2(*b*)), indicating the eye had satisfactory perfusions.

2.2 Histology and Imaging. The ONH and surrounding sclera were isolated using a 14-mm-diameter circular trephine. The tissues were placed in 30% sucrose overnight for cryoprotection, flash-frozen in optimum cutting temperature compound (Tissue Plus, Fisher Healthcare, Houston, TX), and sectioned coronally at 16 μm thickness with a cryostat (Leica CM3050S) [32,33]. Both fluorescence microscopy (FM) and instant polarized light microscopy (IPOL) images were then acquired of each section using a commercial inverted microscope (IX83, Olympus, Tokyo, Japan) to visualize the vessels and collagen, respectively. Note that each FM/IPOL image pair was colocalized to each other as they were acquired right after the other separated only by the motorized filter switch. A 4× strain-free objective (UPLFLN 4XP, Olympus, Tokyo, Japan) was used for both FM and IPOL. A Cy3/TRITC filter set (545/605 nm, Olympus U-3N49004) was used for FM to match the excitation/emission profiles of Dil. IPOL was implemented as described recently [34].

2.3 Three-Dimensional Vascular Network Reconstruction. The stack of IPOL images was registered as described elsewhere [35,36]. Briefly, this was done manually using AVIZO (version 9.1, FEI; Thermo Fisher Scientific) based on tissue edges and fiducial marks made on the sclera and dura before embedding. The set of transformations (translations and rotation) from the IPOL stack registration were then applied to the FM image stack. Thus, an FM/IPOL image pair remained colocalized. A 3D rendered volume of the ONH vasculature is shown in Fig. 3. In addition, we identified the location of the LC based on the registered IPOL images [33,37]. Since the FM/IPOL image stacks were colocalized, the location of the LC identified from IPOL images can be applied to the FM images to identify the vessels in the LC [38].

The registered set of FM images was segmented (Fig. 4) using a semi-automated algorithm based on the Hessian-based Frangi vesselness filter and hysteresis thresholding [39–41]. The binarized images were carefully checked and small corrections were applied if necessary. These were, for example, at some vessel bifurcations because the Frangi filter parameters were selected to optimize accuracy in the main vessel segments and therefore sometimes led to minor over or under-segmentations in bifurcations. Also, because the fluorescent label marked the tissues of the wall, not the lumen, sometimes we had to "fill-in" the vessel. After reconstruction we did a second evaluation of the vessels, checking for continuity and especially for any indication that there may have been clots, poor labeling, or leaks that could have affected the visualization and reconstruction. We observed that sometimes vessel segments exhibited uneven brightness, individually, or as a small region, but these were not difficult to identify and mark reliably once the stack had been assembled. Again, for us to consider the perfusion satisfactory, as was the case for the eye presented in this paper, there had to be no evidence of mislabeled vessels (dark patches) or dye leaks in the vasculature. We recognize that there will always be some degree of uncertainty about the methods and whether this guarantee that every blood vessel is captured. We address this in the discussion.

The vessel network was then skeletonized using the built-in "auto-skeletonization" algorithm in AVIZO (version 9.1, FEI; ThermoScientific) and converted into a 3D graph, with all vessels connected except at the boundaries of the vascular network (Fig. 5). This was done in a semi-automatic iterative process that included segmentation and skeletonization, followed by an analysis and detailed inspection of the skeleton. The results from this analysis

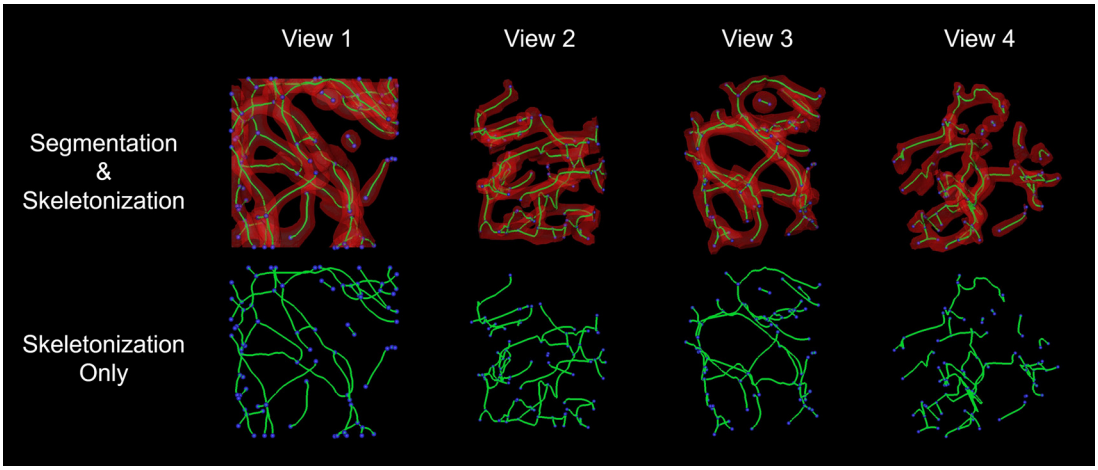

Fig. 5 Illustration of vessel skeletonization. We selected a small region of the LC segmentation and skeletonized it. Shown here are four views of the region. On the top row, the segmentation is shown in semi-transparent red, with green lines and blue spheres representing skeletonized paths and nodes, respectively. On the bottom row, only the skeletonization is shown. The skeletonization follows reasonably well the vessel paths without discernible artifacts. The process of selecting a region of the LC based on flat planes resulted in segments of the vessel that did not connect with the rest of the vasculature. These appear as "islands" in the figure. The vasculature segmentation of the whole lamina had no islands or terminal points within the lamina region. The islands are useful to illustrate that the skeletonization algorithm dealt fine with discontinuities in the segmentation. (Color version online.)

guided an improved resegmentation and reskeletonization. This sometimes required multiple iterations until we were satisfied that the reconstruction was free of potential artifacts while remaining true to the fluorescence images indicating the vasculature. We identified the vessels in the LC region based on the presence of collagen beams [33,37]. The terminal points at the boundaries of the vascular network were grouped based on the anatomic characteristics of the ONH [10,42]. The terminal points were labeled according to their location and likely role. For example, vessel terminal points at the canal periphery are thought to correspond to blood flow inlets from the feeder's vessels in the peripapillary sclera [28,43,44]. Conversely, vessel terminal points at the center are thought to correspond with outlets for blood drainage through the central retinal vein [43]. Terminal points at the anterior and posterior boundaries of the reconstructed volume correspond with anastomoses directly linking the region with the prelaminar and retro-laminar regions.

2.4 Quantification of Vascular Geometry. Each vessel segment was defined as an unbranched tract between two branch points or between a branch point and a terminal point. We characterized four geometric parameters of the segments: length, tortuosity, inclination, and polar orientation. The parameter definitions are illustrated in Fig. 6. The implications of these parameters are detailed in the Discussion section.

3 Results

The 3D reconstructed vascular network of the ONH is shown in Fig. 7, with the vessels in the LC region highlighted. The entire vascular network consisted of 12,966 vessel segments, 7989 branching points, and 1100 terminal points at the network boundaries. Specifically, the numbers of terminal points at the periphery, center, prelaminar, and retro-laminar boundaries were 409, 53, 159, and 479, respectively.

The quantitative analysis of the four geometric parameters of the vessels of the entire ONH is shown in Fig. 8. No obvious spatial patterns emerged when we visualized the vessels colored according to each of the parameters, although it was possible to fit well functional forms to the frequency distribution of each of the parameters. The frequency histograms show that the majority of vessels were short and fairly straight, and primarily oriented toward the coronal plane. The difference in the frequency between the radially and circumferentially aligned vessels was minimal. The quartiles and functional fits of each parameter are summarized in Table 1.

4 Discussion

Our goal was to introduce a workflow that allows reconstruction and morphological analysis of the 3D vascular network of the ONH, including deep tissues within and behind the LC, and feeder vessels from the peripapillary sclera. We have described the workflow and demonstrated that it could be used successfully by showing the 3D reconstruction of the vessels of a monkey ONH.

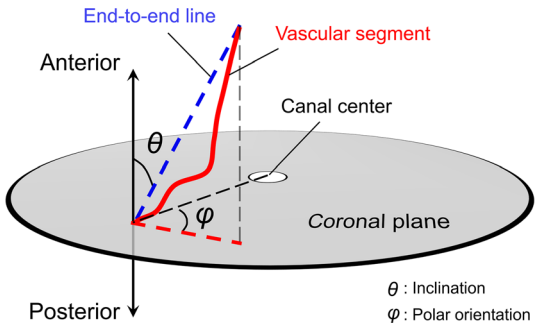

Fig. 6 Diagram illustrating the definition of four geometric parameters of a vascular segment: length, tortuosity, inclination, and polar orientation. The *length* was measured as the path length (red solid line) of the vascular segment. *Tortuosity* ($\geq$1) was calculated as the ratio of the path length to the end-to-end distance (blue dashed line). Tortuosity = 1 indicates that the vessel is straight. *Inclination* ($0 \leq \theta \leq 90$ deg) was measured as the angle between the end-to-end line and the anterior-posterior axis. $\theta = 90$ deg indicates that the vessel is oriented within the coronal plane. *Polar orientation* ($0 \leq \varphi \leq 90$ deg) was measured as the angle of the vessel projection on the coronal plane (red dashed line) relative to the canal center. $\varphi = 0$ deg indicates that the vessel is aligned radially toward/from the canal center, whereas $\varphi = 90$ deg indicates that the vessel is aligned circumferentially. (Color version online.)

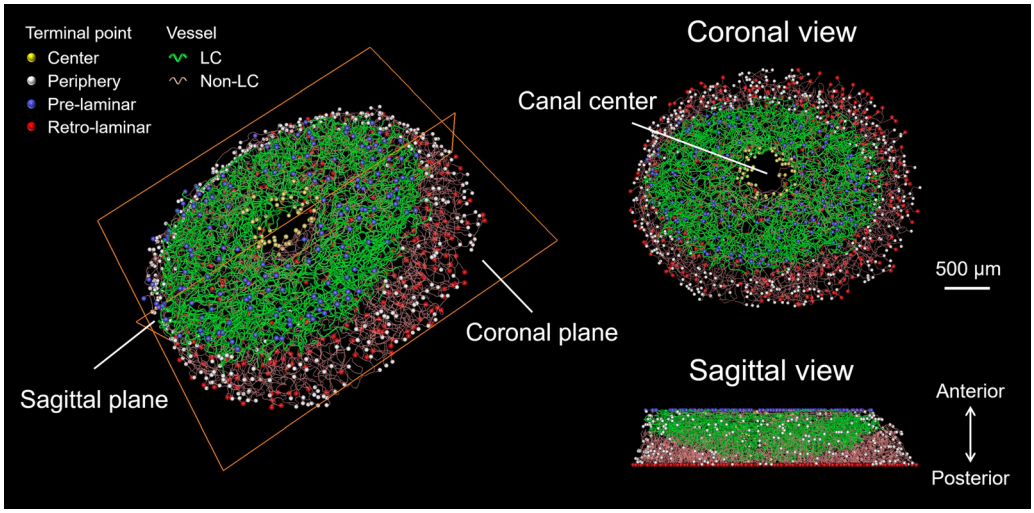

Fig. 7 3D reconstructed ONH vascular network. The vessels in the LC region are shown thick and colored green, with the remaining vessels shown thin and colored pink. The entire vascular network consisted of 12,966 vascular segments, 7989 branching points, and 1100 terminal points at the network boundaries. The terminal points were colored white at the periphery, yellow at the center, lavender at the prelaminar boundary, and red at the retro-laminar boundary, respectively. The gap in the center corresponds to the locations of the central retinal artery and vein, which were excluded in this study. Note that the 3D view on the left is perspective without a scale bar and that the coronal and sagittal views are orthographic and share the same 500-μm scale bar. (Color version online.)

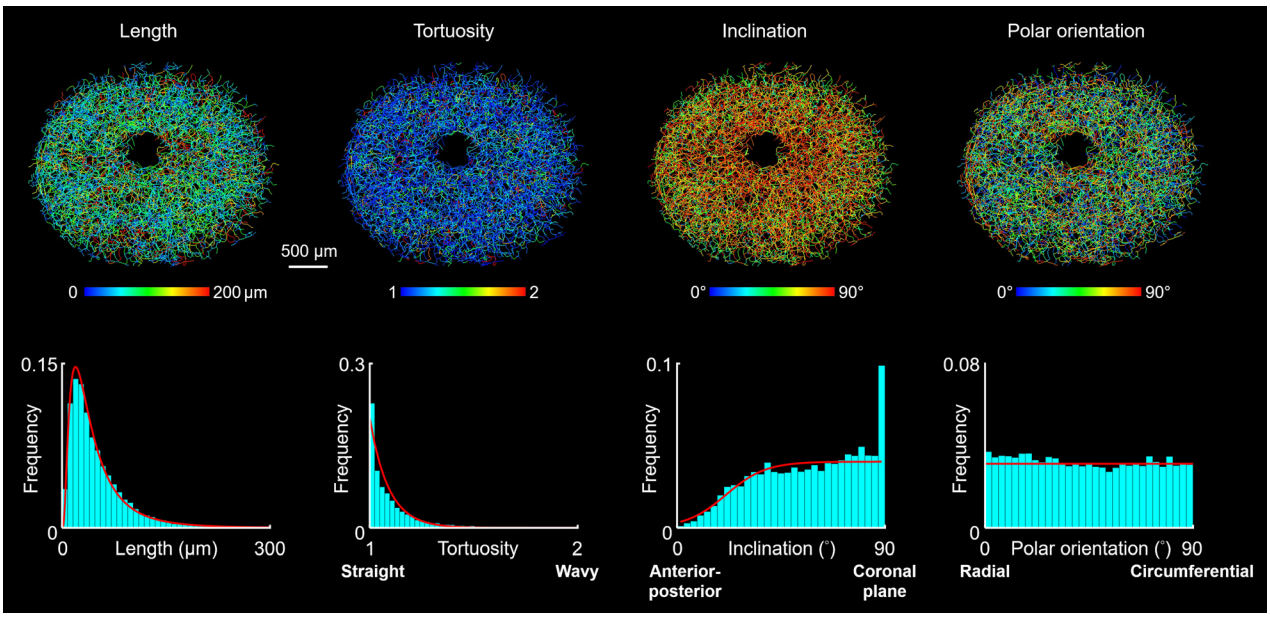

Fig. 8 Characterization of the four geometric parameters (length, tortuosity, inclination, and polar orientation) of the vessels of the entire ONH. *Top row*: Vessels of the ONH shown from the front in coronal view colored according to length, tortuosity, inclination, and polar orientation. The color patterns show that these characteristics were nonuniform throughout the entire network, with no obvious patterns. *Bottom row:* The distribution of the lengths followed a lognormal distribution (μ [mean of logarithmic values] = 3.6 μm, σ [standard deviation of logarithmic values] = 0.8 μm), where the mode (i.e., the highest frequency) was calculated as 19.4 μm (about 40% of the average length) and the skewness is 1.9. The distribution of the tortuosities followed an exponential decay (λ [rate parameter] = 11), where 95% of the vessels had a tortuosity less than 1.46. The frequency of the inclination increased rapidly from 0 deg to 45 deg, slowly thereafter, and spiked at 90 deg. Polar orientation followed a nearly uniform distribution. (Color version online.)

Analysis of the vessels reveals information on the vessel length, tortuosity, inclination, and polar orientation that has not been available from previous techniques. This information is essential to understand ONH hemodynamics and its potential role in physiology, pathology, and vision loss. Before we go any further, we remind readers that the measurements reported herein were obtained from a single eye, and thus that it is impossible to know how general they are. More eyes must be studied before general conclusions can be drawn. Our intent in this work was to illustrate the workflow and the value that it brings to the study of ONH architecture and hemodynamics. We are not aware of publications providing detailed information on ONH vessels that we report. Below we discuss our findings concerning each geometric parameter, why they are important and worthy of study,

Table 1 Quartiles and functional fits of the vessel geometric parameters

	25th percentile	50th percentile	75th percentile	Curve fit models		Fitted parameters
Length (μm)	22	38	66	Lognormal	$\frac{1}{x\sigma\sqrt{2\pi}}e^{-\frac{(\ln x-\mu)^2}{2\sigma^2}}$	$\mu=3.6$; $\sigma=0.8$
Tortuosity	1.02	1.06	1.14	Exponential	$\lambda e^{-\lambda(x-x_0)}, x_0=1$	$\lambda=11$
Inclination (deg)	39	60	78	Logistic	$\frac{L}{1+e^{-k(x-x_{50})}}$	$L=0.04$; $x_{50}=21$; $k=0.12$
Polar orientation (deg)	20	43	67	Uniform	$\frac{1}{x_{\max}-x_{\min}}$	$x_{\min}=0$; $x_{\max}=90$

For reference, the LC is about 3500 μm in diameter, 300 μm in thickness, and about 600 μm from top to bottom (height is larger than thickness because the LC is curved). This means that the median vessel segment is about 1% of LC diameter and 12% of its thickness [45]. Tortuosity varies from 1 for a straight segment to infinity. For comparison, vessels in the porcine ONH have tortuosities from 1 to 1.35 [2]. In terms of the interpretation of the fitted parameters: the logistic model is a function to generate an S-shaped curve, where x_{50} is the x value of the midpoint, k is the steepness of the curve, L is the maximum value of the curve. The parameters $x_{\min}$, $x_{\max}$ of the uniform model are values at the extremes of the range.

Table 2 Comparison of the vessel tortuosity in the ONH with other vascular beds

		Vessel tortuosity			
Tissue	Species	25th percentile	50th percentile	75th percentile	References
ONH	Monkey	1.02	1.06	1.14	This work
LC	Pig	1.07	1.17	1.20	[2]
Brain	Mouse	—	1.07	—	[46]
Retina	Human	—	1.08	1.09	[47]
Kidney	Human	1.07–1.08	1.11–1.13	1.15–1.23	[48]
Spleen	Human	1.56	1.73	2.20	[48]

and suggest potential implications if the findings indeed generalize.

Tortuosity followed an exponential distribution. A comparison of the vessel tortuosity in the ONH with other vascular beds is shown in Table 2. We found that the vessel tortuosity in the monkey ONH, as measured herein, was similar to that in the pig LC [2], the mouse brain [46], the human retina [47], and kidney [48], but smaller than that in the human spleen [48]. Most vessels in the network were fairly straight, but tortuous vessels also existed. Blood flow in tortuous vessels is often lower than that in straight ones, particularly for large vessels; however, tortuous vessels may have some advantages. First, increased tortuosity may bring vessels into closer proximity to the tissues that they nourish, improving overall nutrition and oxygen exchange [49]. Second, vessel tortuosity may provide "slack" that mitigates against reduced blood flow and structural damage caused by excessive distortion under elevated intraocular pressure or changes in gaze position [2,50]. Thus, it seems reasonable that the ONH will exhibit a mix of tortuous and straight vessels, depending on the local needs and biomechanical environment.

Note that tortuosity is a relative concept. A vessel with a tortuosity of 1.0 is straight. Otherwise, it has some tortuosity. Values of tortuosity that determine if a vessel is considered tortuous or not are thus potentially different between tissues or conditions. As shown in Table 2, vessel tortuosity in this work is in line with vessel tortuosity in other tissues and species. Whether vessel tortuosity contributes to making the ONH more susceptible to reduced perfusion or hypoxia is still unknown as it will depend on a large number of factors.

Vessel length followed a lognormal distribution with skewness larger than 1. This means that the majority of vascular lengths were shorter than the mean length. A network formed by short vessels may be more interconnected and robust to vascular occlusion than one formed by long vessels. A comparison of the vessel length in the ONH with other vascular beds is shown in Fig. 9.

Inclination followed a logistic curve. The curve increased rapidly from 0 deg to 45 deg, and smoothly thereafter. There was a spike at 90 deg. The spike likely results from using a relatively thick section (16 μm) to reconstruct the vascular network. This is discussed in more detail later. In terms of the implications, it seems reasonable to expect that vessel sensitivity to mechanical insult depends on the relative orientations of the insult and the vessel [52,53]. For instance, a vessel's compression in the direction perpendicular to its axis might result in a larger flow reduction than a compression longitudinally. Thus, if the ONH is subjected to intraocular pressure-related compression along the anterior-posterior direction [54–57], vessels oriented in the coronal plane (perpendicular to the compressive insult) may be affected more than vessels oriented in the anterior-posterior direction.

The inclination of the ONH vessels may also influence their visibility in imaging. This is crucial to consider because many of the techniques available for imaging the ONH vasculature in vivo have biases in the vessel visibility and flow measurement sensitivity depending on the vessel inclination. For instance, techniques based on Doppler have maximum sensitivity when the vessel (and flow) axis is aligned with the imaging axis. When imaged from the front, as is most common in optical coherence tomography angiography and ultrasound, the techniques would preferentially visualize anterior-posterior vessels and flow [58–60]. Conversely, techniques based on speckle autocorrelation are thought to have higher resolving power in the plane perpendicular to the laser beam, and thus may better visualize vessels and flow in the coronal plane [61–63]. Therefore, a better understanding of the inclination of the ONH vessels is crucial for properly interpreting in vivo data.

Polar orientation followed a nearly uniform distribution. The difference in the frequency between the radially and circumferentially aligned vessels was minimal. Such a slight difference is unlikely to be biomechanically meaningful and impactful. Our finding suggests that the circumferential flow may be as substantial as the radial one. This may facilitate blood circulation in the ONH region, and potentially make it more robust to compression-induced blockage. Our statements about flow and robustness, however, are speculation and must be verified.

We believe that there are many potential applications of our work. We would like to highlight four: First, the 3D reconstructed vascular network will allow modeling eye-specific ONH blood flow and oxygen concentration. This would be more physiologically accurate than what can be considered in 2D generic models

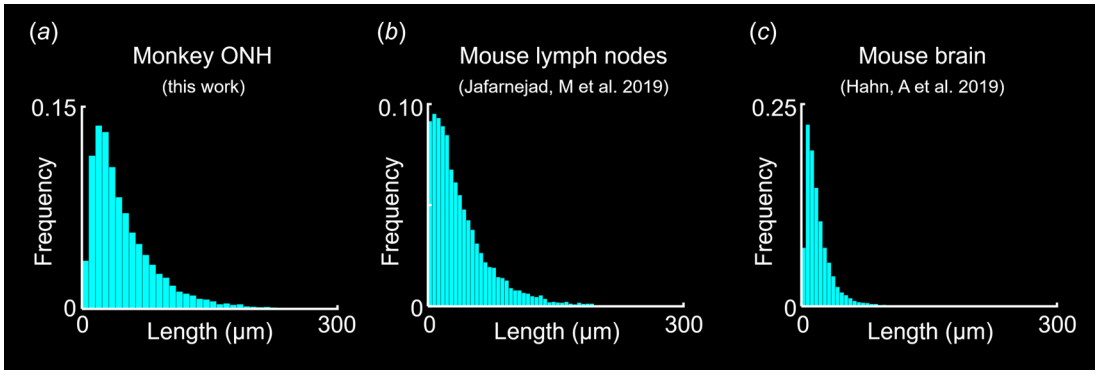

Fig. 9 Comparison of the vessel length between (*a*) the monkey optic nerve head, (*b*) the mouse lymph nodes [51], and (*c*) the mouse brain [46]. The vessel length consistently followed a lognormal distribution. The vessels in the monkey ONH were longer than in other species and organs. Panels (*b*) and (*c*) were replotted to simplify comparison. Note the similarity in the distribution shape, despite the differences due to tissue and species.

[52,53,64,65]. Our reconstructions and analysis will allow evaluating the physiological accuracy of simplified/generic models, and the development of improved ones. Second, the models derived from our vascular network can be used to understand the effects on ONH hemodynamics of tissue distortions, for instance, due to changes in intraocular pressure or cerebrospinal fluid pressure, or due to changes in gaze position [49,55,66,67]. Predictions made with detailed specimen-specific models can then be better compared with experimental data than generic models. Third, our integrated imaging technique, i.e., FM and IPOL, allowed us to reconstruct both the vessels and collagen in the ONH. It is thus possible to evaluate the spatial relationship between the vascular and collagenous networks. Other vessel visualization techniques, such as plastic casts, have required "digestion" of the tissues for visualization [28,29]. This makes it impossible to determine accurately the inter-relationship between vessels and nonvessels tissues. The combined vessels and collagen information from our workflow allow precisely locating the vessels. This, in turn, allows distinguishing vessels inside/outside the canal, and vessels within or outside LC collagen beams. These will likely have important implications on the sensitivity of the vessels to distortion and their proximity to the neural tissues [38]. Fourth, the techniques for visualizing and characterizing ONH vasculature in vivo have major limitations. The reconstructions and morphologic parameters from our workflow can provide the essential "ground truth" to assess and optimize other techniques. All of these applications will benefit from the detailed reconstruction methods we present and are evidence of the great potential that our technique has to help understand the interactions between morphological, hemodynamic, and biomechanical factors influencing blood flow and oxygenation in the ONH.

It is important to acknowledge the limitations of this work. A salient one, noted above, is that we have presented measurements from a single eye. Our work, therefore, serves as a demonstration of what can be done. Although our measures of the vessel tortuosity and length were generally consistent with those of other vascular beds, our numbers were obtained from a single ONH. Given the high intereye variability in other aspects of ONH morphology, readers should be cautious and not assume that our findings are general. There are also limitations of the 3D vascular network reconstruction workflow. Dye perfusion postmortem may not reach all vessel segments. This could result from intravascular clotting or insufficient perfusate volume. To prevent intravascular clotting, efforts were made to minimize the time interval between animal death and perfusion. In addition, the vessels were flushed with extensive phosphate-buffered saline over a long time to remove the residual blood clots. To ensure sufficient labeling, we used a large volume of dye to perfuse. The examination using a dissecting fluorescence microscope showed strong fluorescence signals in retinal and choroidal vessels, suggesting sufficient vessel perfusion. We did not observe gaps or recognize regions blocked by clots, which does not mean that they did not exist but does strongly suggest that they would be small and not abundant. It is worth noting that other ex vivo perfusion techniques have equivalent or worse risks. For example, vascular casting is well-known to be affected by the solution viscosity that may prevent full perfusion into smaller vessels [28,29].

Artifacts may result from fixation or sectioning, including tissue distortion or shrinkage. However, we have shown previously that our method of formalin fixation has minimal effects on the gross size or shape of ocular tissues [32,33]. It is unclear how it may affect the vasculature within. Artifacts may also result from registering histological section images. We could have used the central retinal vessels in the FM as continuous vascular features for registration. However, we were worried that this could lead to artefactually aligning other vessels in these images. To avoid this problem, we registered the stacks using the IPOL images of collagen. Specifically, we used the tissue edges and other recognizable structures to align them, and then applied the set of transformations from the IPOL stack registration to the FM image stack. This process is time-consuming and may introduce misalignment due to subjective evaluation of the registration. We could use fiducial markers to help register images and account for warping [68]. Note that these artifacts are not necessarily worse and are potentially smaller than with other imaging techniques. For example, in vivo optical coherence tomography suffers substantial artifacts caused by motion, projections of superficial blood flow, or shadows from opaque objects anterior to the retina (e.g., vitreous floaters, pupil boundary) [69].

Artifacts may also result from the segmentation and skeletonization steps. Unevenly or sometimes slightly discontinuous labeling increased the difficulty in segmentation. Hessian filter and hysteresis thresholding provided excellent starting points for vessel contour enhancement but with limited success on uneven labels and at anastomoses. Therefore, it was still necessary to manually "clean" and "bridge" segments. Particularly, time consuming was identifying and cleaning out-of-plane vessel discontinuities. It was also crucial to ensure the smoothness of the segmentations because this impacts the skeletonization. Intervening on this could potentially affect the vessel widths or diameters, and therefore we decided to not report vessel diameters. Problems with the skeletonization often lead to many artefactual short segments forming small loops or fanning out. These were not observed in the skeletonization reported herein, in large part because of our use of an iterative algorithm that ensured they were eliminated. However, the general problem of skeletonization in 3D remains a challenge and the same algorithm can perform differently in other images and networks. Future studies

should be careful and not assume that the skeletonization is accurate.

As noted above, the section thickness may affect the reconstructions, and it is thus an important consideration. When choosing the thickness, there are tradeoffs between the advantages of thick and thin sections. Thicker sections suffer less from distortion and reduce the workload. Thinner sections allow more detailed reconstruction, allowing distinguishing better the vessel plane and especially the inclination of short vessels. In this study, the section thickness was chosen as 16 μm, resulting in 58 sections through the monkey ONH. Of these, 29 sections were selected for reconstruction. With this depth resolution, any two vessels with a gap distance of less than 16 μm in depth were connected, and vessels shorter than 45 μm and an inclination of more than 80 deg were regarded as in the coronal plane. This explains the sharp increase in vessel frequency at 90 deg inclination (in the section plane). Reducing the section thickness would improve the fidelity of the 3D reconstructed vascular network. For example, techniques like a tape transfer system can be used to reduce the minimal section thickness to single digit μm [70]. Alternatively, future work could use techniques that can provide depth information, such as confocal microscopy, or structured light illumination [2,]. There are also block face imaging and serial electron microscopy tools that can provide exquisite resolution in the order of nm [71,72]. Those techniques, however, tend to be substantially slower and expensive and thus are rarely used for analyzing a large set of sections as we have done here.

Our analysis did not provide information on the vessel diameters. Postmortem vessel diameter may differ from that in vivo due to the absence of blood pressure and/or tissue swelling postmortem. An additional challenge is that many vessels are inside the connective tissue beams [2], which may further complicate the diameter changes postmortem. Inside the micromechanical environment of collagenous beams, the diameter of the vasculature may be related to the sensitivity of perfusion when intraocular pressure changes. Future work could examine this issue using other methods to label vessels of the ONH, which may potentially require more complex and specific labeling techniques and likely slower imaging.

Overall, we demonstrated a histological imaging workflow allowing reconstruction and morphological analysis of the 3D vascular network of the ONH. A similar approach can be used to reconstruct vascular networks in eyes of different ages and diseased eyes to further understand age- and disease-related morphological changes in the ONH vasculature.

Funding Data

- National Institutes of Health (Grant Nos. R01-EY023966, R01-EY028662, R01-EY031708, P30-EY008098, and T32-EY017271; Funder ID: 10.13039/100000053).
- National Institute of Child Health and Human Development (Grant Nos. R01-HD045590 and R01-HD083383; Funder ID: 10.13039/100000071).
- Eye and Ear Foundation (Pittsburgh, PA), Research to Prevent Blindness (Award: Stein Innovation Award; Funder ID: 10.13039/100001818).

Declarations

Bryn L. Brazile was at the University of Pittsburgh when he contributed to this work. He is now at Baxter; Other authors have nothing to disclose.

References

[1] Stein, J. D., Khawaja, A. P., and Weizer, J. S., 2021, "Glaucoma in Adults—Screening, Diagnosis, and Management: A Review," JAMA, **325**(2), pp. 164–174.

[2] Brazile, B. L., Yang, B., Waxman, S., Lam, P., Voorhees, A. P., Hua, Y., Loewen, R. T., Loewen, N. A., Rizzo, J. F., III, Jakobs, T. C., and Sigal, I. A., 2020, "Lamina Cribrosa Capillaries Straighten as Intraocular Pressure Increases," Invest. Ophthalmol. Visual Sci., **61**(12), pp. 2–2.

[3] Lieberman, M. F., Maumenee, A. E., and Green, W. R., 1976, "Histologic Studies of the Vasculature of the Anterior Optic Nerve," Am. J. Ophthalmol., **82**(3), pp. 405–423.

[4] Zhang, L., Albon, J., Jones, H., Gouget, C. L., Ethier, C. R., Goh, J. C., and Girard, M. J., 2015, "Collagen Microstructural Factors Influencing Optic Nerve Head Biomechanics," Invest. Ophthalmol. Visual Sci., **56**(3), pp. 2031–2042.

[5] Midgett, D. E., Jefferys, J. L., Quigley, H. A., and Nguyen, T. D., 2020, "The Inflation Response of the Human Lamina Cribrosa and Sclera: Analysis of Deformation and Interaction," Acta Biomater., **106**(1), pp. 225–241.

[6] Pavlatos, E., Ma, Y., Clayson, K., Pan, X., and Liu, J., 2018, "Regional Deformation of the Optic Nerve Head and Peripapillary Sclera During IOP Elevation," Invest. Ophthalmol. Visual Sci., **59**(8), pp. 3779–3788.

[7] Voorhees, A. P., Jan, N.-J., Austin, M. E., Flanagan, J. G., Sivak, J. M., Bilonick, R. A., and Sigal, I. A., 2017, "Lamina Cribrosa Pore Shape and Size as Predictors of Neural Tissue Mechanical Insult," Invest. Ophthalmol. Visual Sci., **58**(12), pp. 5336–5346.

[8] Voorhees, A. P., Jan, N.-J., and Sigal, I. A., 2017, "Effects of Collagen Microstructure and Material Properties on the Deformation of the Neural Tissues of the Lamina Cribrosa," Acta Biomater., **58**, pp. 278–290.

[9] Quigley, H. A., 2005, "Glaucoma: Macrocosm to Microcosm the Friedenwald Lecture," Invest. Ophthalmol. Visual Sci., **46**(8), pp. 2663–2670.

[10] Sigal, I. A., and Ethier, C. R., 2009, "Biomechanics of the Optic Nerve Head," Exp. Eye Res., **88**(4), pp. 799–807.

[11] Harris, A., Kagemann, L., Ehrlich, R., Rospigliosi, C., Moore, D., and Siesky, B., 2008, "Measuring and Interpreting Ocular Blood Flow and Metabolism in Glaucoma," Can. J. Ophthalmol., **43**(3), pp. 328–336.

[12] Moore, D., Harris, A., Wudunn, D., Kheradiya, N., and Siesky, B., 2008, "Dysfunctional Regulation of Ocular Blood Flow: A Risk Factor for Glaucoma?," Clin. Ophthalmol. (Auckland, N.Z.), **2**(4), pp. 849–861.

[13] Galassi, F., Giambene, B., and Varriale, R., 2011, "Systemic Vascular Dysregulation and Retrobulbar Hemodynamics in Normal-Tension Glaucoma," Invest. Ophthalmol. Visual Sci., **52**(7), pp. 4467–4471.

[14] Kanakamedala, P., Harris, A., Siesky, B., Tyring, A., Muchnik, M., Eckert, G., and Tobe, L. A., 2014, "Optic Nerve Head Morphology in Glaucoma Patients of African Descent is Strongly Correlated to Retinal Blood Flow," Br. J. Ophthalmol., **98**(11), pp. 1551–1554.

[15] Hayreh, S. S., 1997, "Factors Influencing Blood Flow in the Optic Nerve Head," J. Glaucoma, **6**(6), pp. 412–425.

[16] Sigal, I. A., Wang, B., Strouthidis, N. G., Akagi, T., and Girard, M. J., 2014, "Recent Advances in OCT Imaging of the Lamina Cribrosa," Br. J. Ophthalmol., **98**(Suppl 2), pp. ii34–ii39.

[17] Numa, S., Akagi, T., Uji, A., Suda, K., Nakanishi, H., Kameda, T., Ikeda, H. O., and Tsujikawa, A., 2018, "Visualization of the Lamina Cribrosa Microvasculature in Normal and Glaucomatous Eyes: A Swept-Source Optical Coherence Tomography Angiography Study," J. Glaucoma, **27**(11), pp. 1032–1035.

[18] Zhu, J., Bernucci, M. T., Merkle, C. W., and Srinivasan, V. J., 2020, "Visibility of Microvessels in Optical Coherence Tomography Angiography Depends on Angular Orientation," J. Biophotonics, **13**(10), p. e202000090.

[19] Kim, J.-A., Lee, E. J., Kim, T.-W., Yang, H. K., and Hwang, J.-M., 2021, "Comparison of Optic Nerve Head Microvasculature Between Normal-Tension Glaucoma and Nonarteritic Anterior Ischemic Optic Neuropathy," Invest. Ophthalmol. Visual Sci., **62**(10), p. 15.

[20] Yu, J., Lavery, L., and Kim, K., 2018, "Super-Resolution Ultrasound Imaging Method for Microvasculature In Vivo With a High Temporal Accuracy," Sci. Rep., **8**(1), pp. 1–11.

[21] Christensen-Jeffries, K., Couture, O., Dayton, P. A., Eldar, Y. C., Hynynen, K., Kiessling, F., O'Reilly, M., Pinton, G. F., Schmitz, G., Tang, M.-X., Tanter, M., and van Sloun, R. J. G., 2020, "Super-Resolution Ultrasound Imaging," Ultrasound Med. Biol., **46**(4), pp. 865–891.

[22] Chen, Q., Yu, J., Lukashova, L., Latoche, J. D., Zhu, J., Lavery, L., Verdelis, K., Anderson, C. J., and Kim, K., 2020, "Validation of Ultrasound Super-Resolution Imaging of Vasa Vasorum in Rabbit Atherosclerotic Plaques," IEEE Trans. Ultrason. Ferroelectr. Freq. Control, **67**(8), pp. 1725–1729.

[23] Qian, X., Kang, H., Li, R., Lu, G., Du, Z., Shung, K. K., Humayun, M. S., and Zhou, Q., 2020, "In Vivo Visualization of Eye Vasculature Using Super-Resolution Ultrasound Microvessel Imaging," IEEE Trans. Biomed. Eng., **67**(10), pp. 2870–2880.

[24] Duong, T. Q., Pardue, M. T., Thulé, P. M., Olson, D. E., Cheng, H., Nair, G., Li, Y., Kim, M., Zhang, X., and Shen, Q., 2008, "Layer-Specific Anatomical, Physiological and Functional MRI of the Retina," NMR Biomed., **21**(9), pp. 978–996.

[25] Voorhees, A. P., Ho, L. C., Jan, N.-J., Tran, H., van der Merwe, Y., Chan, K., and Sigal, I. A., 2017, "Whole-Globe Biomechanics Using High-Field MRI," Exp. Eye Res., **160**, pp. 85–95.

[26] Ho, L. C., Sigal, I. A., Jan, N.-J., Squires, A., Tse, Z., Wu, E. X., Kim, S.-G., Schuman, J. S., and Chan, K. C., 2014, "Magic Angle–Enhanced MRI of Fibrous Microstructures in Sclera and Cornea With and Without Intraocular Pressure Loading," Invest. Ophthalmol. Visual Sci., **55**(9), pp. 5662–5672.

[27] Ho, L. C., Sigal, I. A., Jan, N.-J., Yang, X., van der Merwe, Y., Yu, Y., Chau, Y., Leung, C. K., Conner, I. P., Jin, T., Wu, E. X., Kim, S.-G., Wollstein, G., Schuman, J. S., and Chan, K. C., 2016, "Non-Invasive MRI Assessments of Tissue Microstructures and Macromolecules in the Eye Upon Biomechanical or Biochemical Modulation," Sci. Rep., **6**(1), p. 32080.

[28] Mackenzie, P. J., and Cioffi, G. A., 2008, "Vascular Anatomy of the Optic Nerve Head," Can. J. Ophthalmol., **43**(3), pp. 308–312.

[29] Zhao, D.-Y., and Cioffi, G. A., 2000, "Anterior Optic Nerve Microvascular Changes in Human Glaucomatous Optic Neuropathy," Eye, **14**(3), pp. 445–449.
[30] The Association for Research in Vision and Ophthalmology, 2022, "Statement for the Use of Animals in Ophthalmic and Vision Research," The Association for Research in Vision and Ophthalmology, Rockville, MD, accessed Feb. 28, 2022, https://www.arvo.org/About/policies/statement-for-the-use-of-animals-in-ophthalmic-and-vision-research/
[31] Li, Y., Song, Y., Zhao, L., Gaidosh, G., Laties, A. M., and Wen, R., 2008, "Direct Labeling and Visualization of Blood Vessels With Lipophilic Carbocyanine Dye DiI," Nat. Protoc., **3**(11), pp. 1703–1708.
[32] Tran, H., Jan, N.-J., Hu, D., Voorhees, A., Schuman, J. S., Smith, M. A., Wollstein, G., and Sigal, I. A., 2017, "Formalin Fixation and Cryosectioning Cause Only Minimal Changes in Shape or Size of Ocular Tissues," Sci. Rep., **7**(1), pp. 1–11.
[33] Jan, N.-J., Grimm, J. L., Tran, H., Lathrop, K. L., Wollstein, G., Bilonick, R. A., Ishikawa, H., Kagemann, L., Schuman, J. S., and Sigal, I. A., 2015, "Polarization Microscopy for Characterizing Fiber Orientation of Ocular Tissues," Biomed. Optics Express, **6**(12), pp. 4705–4718.
[34] Yang, B., Lee, P. Y., Hua, Y., Brazile, B., Waxman, S., Ji, F., Zhu, Z., and Sigal, I. A., 2021, "Instant Polarized Light Microscopy for Imaging Collagen Microarchitecture and Dynamics," J. Biophotonics, **14**(2), p. e202000326.
[35] Gogola, A., Jan, N.-J., Lathrop, K. L., and Sigal, I. A., 2018, "Radial and Circumferential Collagen Fibers Are a Feature of the Peripapillary Sclera of Human, Monkey, Pig, Cow, Goat, and Sheep," Invest. Ophthalmol. Visual Sci., **59**(12), pp. 4763–4774.
[36] Jan, N.-J., Brazile, B. L., Hu, D., Grube, G., Wallace, J., Gogola, A., and Sigal, I. A., 2018, "Crimp Around the Globe; Patterns of Collagen Crimp Across the Corneoscleral Shell," Exp. Eye Res., **172**, pp. 159–170.
[37] Jan, N.-J., Lathrop, K., and Sigal, I. A., 2017, "Collagen Architecture of the Posterior Pole: High-Resolution Wide Field of View Visualization and Analysis Using Polarized Light Microscopy," Invest. Ophthalmol. Visual Sci., **58**(2), pp. 735–744.
[38] Waxman, S., Brazile, B. L., Yang, B., Lee, P.-Y., Hua, Y., Gogola, A. L., Lam, P., Voorhees, A. P., Rizzo, J. F., Jakobs, T. C., and Sigal, I. A., 2022, "Lamina Cribrosa Vessel and Collagen Beam Networks Are Distinct," Exp. Eye Res., **215**, p. 108916.
[39] Kroon, D.-J., 2022, "Hessian Based Frangi Vesselness Filter," MATLAB Central File Exchange, accessed Mar. 17, 2022, https://www.mathworks.com/matlabcentral/fileexchange/24409-hessian-based-frangi-vesselness-filter
[40] Campbell, I. C., Coudrillier, B., Mensah, J., Abel, R. L., and Ethier, C. R., 2015, "Automated Segmentation of the Lamina Cribrosa Using Frangi's Filter: A Novel Approach for Rapid Identification of Tissue Volume Fraction and Beam Orientation in a Trabeculated Structure in the Eye," J. R. Soc. Interface, **12**(104), p. 20141009.
[41] Jerman, T., Pernuš, F., Likar, B., and Špiclin, Ž., 2016, "Enhancement of Vascular Structures in 3D and 2D Angiographic Images," IEEE Trans. Med. Imaging, **35**(9), pp. 2107–2118.
[42] Sigal, I. A., Flanagan, J. G., Tertinegg, I., and Ethier, C. R., 2010, "3D Morphometry of the Human Optic Nerve Head," Exp. Eye Res., **90**(1), pp. 70–80.
[43] Hayreh, S. S., 2001, "Blood Flow in the Optic Nerve Head and Factors That May Influence It," Prog. Retinal Eye Res., **20**(5), pp. 595–624.
[44] Hayreh, S. S., 1996, "Blood Supply of the Optic Nerve Head," Ophthalmologica, **210**(5), pp. 285–295.
[45] Yang, H., Downs, J. C., Girkin, C., Sakata, L., Bellezza, A., Thompson, H., and Burgoyne, C. F., 2007, "3-D Histomorphometry of the Normal and Early Glaucomatous Monkey Optic Nerve Head: Lamina Cribrosa and Peripapillary Scleral Position and Thickness," Invest. Ophthalmol. Visual Sci., **48**(10), pp. 4597–4607.
[46] Hahn, A., Bode, J., Krüwel, T., Solecki, G., Heiland, S., Bendszus, M., Tews, B., Winkler, F., Breckwoldt, M. O., and Kurz, F. T., 2019, "Glioblastoma Multiforme Restructures the Topological Connectivity of Cerebrovascular Networks," Sci. Rep., **9**(1), pp. 1–17.
[47] Saraf, S. S., Tyring, A. J., Chen, C.-L., Le, T. P., Kalina, R. E., Wang, R. K., and Chao, J. R., 2019, "Familial Retinal Arteriolar Tortuosity and Quantification of Vascular Tortuosity Using Swept-Source Optical Coherence Tomography Angiography," Am. J. Ophthalmol. Case Rep., **14**, pp. 74–78.
[48] Ágg, B., Szilveszter, B., Daradics, N., Benke, K., Stengl, R., Kolossváry, M., Pólos, M., Radovits, T., Ferdinandy, P., Merkely, B., Maurovich-Horvat, P., and Szabolcs, Z., 2020, "Increased Visceral Arterial Tortuosity in Marfan Syndrome," Orphanet J. Rare Dis., **15**(1), pp. 1–10.
[49] Goldman, D., and Popel, A. S., 2000, "A Computational Study of the Effect of Capillary Network Anastomoses and Tortuosity on Oxygen Transport," J. Theor. Biol., **206**(2), pp. 181–194.
[50] Sibony, P. A., Wei, J., and Sigal, I. A., 2018, "Gaze-Evoked Deformations in Optic Nerve Head Drusen: Repetitive Shearing as a Potential Factor in the Visual and Vascular Complications," Ophthalmology, **125**(6), pp. 929–937.
[51] Jafarnejad, M., Ismail, A., Duarte, D., Vyas, C., Ghahramani, A., Zawieja, D., Celso, C. L., Poologasundarampillai, G., and Moore, J., 2019, "Quantification of the Whole Lymph Node Vasculature Based on Tomography of the Vessel Corrosion Casts," Sci. Rep., **9**(1), pp. 1–11.
[52] Chuangsuwanich, T., Hung, P. T., Wang, X., Liang, L. H., Schmetterer, L., Boote, C., and Girard, M. J. A., 2020, "Morphometric, Hemodynamic, and Biomechanical Factors Influencing Blood Flow and Oxygen Concentration in the Human Lamina Cribrosa," Invest. Ophthalmol. Visual Sci., **61**(4), p. 3.
[53] Chuangsuwanich, T., Birgersson, K. E., Thiery, A., Thakku, S. G., Leo, H. L., and Girard, M. J., 2016, "Factors Influencing Lamina Cribrosa Microcapillary Hemodynamics and Oxygen Concentrations," Invest. Ophthalmol. Visual Sci., **57**(14), pp. 6167–6179.
[54] Sigal, I. A., Flanagan, J. G., Tertinegg, I., and Ethier, C. R., 2007, "Predicted Extension, Compression and Shearing of Optic Nerve Head Tissues," Exp. Eye Res., **85**(3), pp. 312–322.
[55] Sigal, I. A., Grimm, J. L., Jan, N. J., Reid, K., Minckler, D. S., and Brown, D. J., 2014, "Eye-Specific IOP-Induced Displacements and Deformations of Human Lamina Cribrosa," Invest. Ophthalmol. Visual Sci., **55**(1), pp. 1–15.
[56] Ma, Y., Kwok, S., Sun, J., Pan, X., Pavlatos, E., Clayson, K., Hazen, N., and Liu, J., 2020, "IOP-Induced Regional Displacements in the Optic Nerve Head and Correlation With Peripapillary Sclera Thickness," Exp. Eye Res., **200**, p. 108202.
[57] Ma, Y., Pavlatos, E., Clayson, K., Pan, X., Kwok, S., Sandwisch, T., and Liu, J., 2019, "Mechanical Deformation of Human Optic Nerve Head and Peripapillary Tissue in Response to Acute IOP Elevation," Invest. Ophthalmol. Visual Sci., **60**(4), pp. 913–920.
[58] Yazdanfar, S., Rollins, A. M., and Izatt, J. A., 2000, "Imaging and Velocimetry of the Human Retinal Circulation With Color Doppler Optical Coherence Tomography," Opt. Lett., **25**(19), pp. 1448–1450.
[59] Tranquart, F., Bergès, O., Koskas, P., Arsene, S., Rossazza, C., Pisella, P. J., and Pourcelot, L., 2003, "Color Doppler Imaging of Orbital Vessels: Personal Experience and Literature Review," J. Clin. Ultrasound, **31**(5), pp. 258–273.
[60] Harris, A., Kagemann, L., and Cioffi, G. A., 1998, "Assessment of Human Ocular Hemodynamics," Surv. Ophthalmol., **42**(6), pp. 509–533.
[61] Hormel, T. T., Huang, D., and Jia, Y., 2020, "Artifacts and Artifact Removal in Optical Coherence Tomographic Angiography," Quant. Imaging Med. Surg., **11**(3), pp. 1120–1133.
[62] Wang, L., Cull, G. A., Piper, C., Burgoyne, C. F., and Fortune, B., 2012, "Anterior and Posterior Optic Nerve Head Blood Flow in Nonhuman Primate Experimental Glaucoma Model Measured by Laser Speckle Imaging Technique and Microsphere Method," Invest. Ophthalmol. Visual Sci., **53**(13), pp. 8303–8309.
[63] Liang, Y., Fortune, B., Cull, G., Cioffi, G. A., and Wang, L., 2010, "Quantification of Dynamic Blood Flow Autoregulation in Optic Nerve Head of Rhesus Monkeys," Exp. Eye Res., **90**(2), pp. 203–209.
[64] Causin, P., Guidoboni, G., Malgaroli, F., Sacco, R., and Harris, A., 2016, "Blood Flow Mechanics and Oxygen Transport and Delivery in the Retinal Microcirculation: Multiscale Mathematical Modeling and Numerical Simulation," Biomech. Model. Mechanobiol., **15**(3), pp. 525–542.
[65] Causin, P., Guidoboni, G., Harris, A., Prada, D., Sacco, R., and Terragni, S., 2014, "A Poroelastic Model for the Perfusion of the Lamina Cribrosa in the Optic Nerve Head," Math. Biosci., **257**, pp. 33–41.
[66] Hua, Y., Voorhees, A. P., and Sigal, I. A., 2018, "Cerebrospinal Fluid Pressure: Revisiting Factors Influencing Optic Nerve Head Biomechanics," Invest. Ophthalmol. Visual Sci., **59**(1), pp. 154–165.
[67] Zhu, Z., Waxman, S., Wang, B., Wallace, J., Schmitt, S. E., Tyler-Kabara, E., Ishikawa, H., Schuman, J. S., Smith, M. A., Wollstein, G., and Sigal, I. A., 2021, "Interplay Between Intraocular and Intracranial Pressure Effects on the Optic Nerve Head In Vivo," Exp. Eye Res., **213**, p. 108809.
[68] Sigal, I. A., Flanagan, J. G., Tertinegg, I., and Ethier, C. R., 2005, "Reconstruction of Human Optic Nerve Heads for Finite Element Modeling," Technol. Health Care, **13**(4), pp. 313–329.
[69] Spaide, R. F., Fujimoto, J. G., and Waheed, N. K., 2015, "Image Artifacts in Optical Coherence Angiography," Retina (Philadelphia, Pa.), **35**(11), pp. 2163–2180.
[70] Golubeva, Y. G., Smith, R. M., and Sternberg, L. R., 2013, "Optimizing Frozen Sample Preparation for Laser Microdissection: Assessment of CryoJane Tape-Transfer System®," PLoS One, **8**(6), p. e66854.
[71] Quantock, A. J., Winkler, M., Parfitt, G. J., Young, R. D., Brown, D. J., Boote, C., and Jester, J. V., 2015, "From Nano to Macro: Studying the Hierarchical Structure of the Corneal Extracellular Matrix," Exp. Eye Res., **133**, pp. 81–99.
[72] Boote, C., Sigal, I. A., Grytz, R., Hua, Y., Nguyen, T. D., and Girard, M. J., 2020, "Scleral Structure and Biomechanics," Prog. Retinal Eye Res., **74**, p. 100773.